RSC Advances

PAPER

View Article Online
View Journal | View Issue

Check for updates

Cite this: *RSC Adv.*, 2025, **15**, 5639

Equal volume impregnation–air calcination synthesis of lithium-doped MgO nanoplates for enhanced antibacterial performance†

Xiaoyi Li,[a] Junmei Pu,[a] Yanqun Zu,[a] Yongmei He,[a] Fangdong Zhan,[a] Xi Li[a] and Jiao Zhao *[b]

Received 4th October 2024
Accepted 3rd February 2025

DOI: 10.1039/d4ra07138g

rsc.li/rsc-advances

Magnesium oxide nanomaterials (nano-MgO) have many advantages, such as environmentally benign, high thermal stability, no need of illumination, broad-spectrum antibacterial activity and more. However, its low activity has restricted the application in environmental purification and antibacterial disinfection. Herein, the equal volume impregnation–air calcination method was first used in the synthesis of nano-MgO and a series of nano-MgO with varying amounts of Li doping were prepared to enhance their antibacterial properties. Li doping leads to the distortion of MgO lattice structure and the presence of oxygen vacancies, enhancing oxygen absorption and alkalinity. This enhancement effectively promotes the formation of reactive oxygen species (ROS) and maintains its high chemical reactivity. The Li doped nano-MgO at 100 μg mL^{-1} showed a significant improvement in antibacterial activity, achieving the antibacterial ratio of 99.6% against *Escherichia coli* (*E. coli*). Moreover, the contribution of alkalinity, ROS, physical morphology effect, and dissolved ions (Mg^{2+} and Li^{+}) to the antibacterial ability was further discussed. Especially, the results of dialysis tube test indirectly indicated that ROS played the crucial role in enhancing the antibacterial performance of nano-MgO. This study lays an essential foundation for further investigation into the antibacterial performance and mechanism of nano-MgO.

1. Introduction

Malignant multiplication and widespread dissemination of pathogenic microorganisms have become increasingly threatening to people's health, such as the infections caused by SARS-CoV-2, Monkeypox, *E. coli*, *Streptococcus haemolyticus*, and *Serratia marcescens*.[1–4] It is crucial to deactivate and suppress dangerous germs to slow down the spread of epidemic diseases. Recent research has shown that inorganic nanomaterials include silver and silver derivatives,[5] photocatalysts like TiO_2 and ZnO,[6,7] rare-earth-based complexes[8] and MgO[9] can effectively inactivate disease causing microorganisms. Among these materials, magnesium oxide nanomaterials (nano-MgO) have garnered significant attention from researchers due to its high refractoriness and stability, low cost, environmentally friendly and completely light-independent antibacterial capability. However, nano-MgO still face challenges such as high effective concentration requirements and lower activity levels compared with that of silver-based and photocatalytic materials.[10]

The antibacterial effect of nano-MgO depends on the oxygen vacancies that cause one-electron reduction processes to generate ROS.[11] Additionally, the hydrolysis of nano-MgO' surface results in the production of OH^{-}, which raises the alkalinity in a liquid-phase environment. The results of the previous literature showed that the alkaline environment was available to enhance the chemical stability of ROS.[12] From the above mechanism, how to find a modification method to precisely construct oxygen vacancies in the matrix of nano-MgO for inducing the generation of more ROS and maintaining its high activity is key to enhancing the antibacterial performance of nano-MgO. The orderly arrangement of atoms in the intact lattice structure of MgO makes it difficult to introduce oxygen vacancies. Doping is a useful technique for modifying the perfect lattice structure of MgO. Due to the variation in atomic radius, doping can lead to localized lattice distortion and disorder.[13] The disruption of the lattice structure also triggers the movement of oxygen atoms from their original positions, resulting in the formation of oxygen vacancies. Currently, researchers have designed a series of metal-doped nano-MgO, such as doping Fe,[14,15] Zn,[16,17] Gd,[18] Co,[19] Al,[19] La,[19] Cu,[20] Ag,[21] Ni,[22] Li,[23] and Ti.[23] The above studies have indicated that the metal doping method by regulating doping species and content can successfully introduce oxygen vacancies and enhance the antibacterial properties of nano-MgO. Among them, alkali metal efficiently introduces oxygen vacancies, more

[a]*College of Resources and Environmental Science, Yunnan Agricultural University, Kunming 650201, China*

[b]*Collaborative Innovation Center for Vessel Pollution Monitoring and Control, Dalian Maritime University, Dalian 116026, China. E-mail: zhaojiao@dlmu.edu.cn*

† Electronic supplementary information (ESI) available. See DOI: https://doi.org/10.1039/d4ra07138g

Open Access Article. Published on 19 February 2025. Downloaded on 5/4/2026 11:03:49 AM. This article is licensed under a Creative Commons Attribution-NonCommercial 3.0 Unported Licence.

Open Access Article. Published on 19 February 2025. Downloaded on 5/4/2026 11:03:49 AM. This article is licensed under a Creative Commons Attribution-NonCommercial 3.0 Unported Licence.

importantly, it could enhance the alkalinity of nano-MgO, which contributes to the generation and stability of ROS. Metal-doped nano-MgO along with high alkalinity, plays a significant role in the antibacterial performance. For example, Wang *et al.* prepared a series of metal-doped MgO, including Li, Ti, Zn and Ag.[23–25] Li-doped nano-MgO exhibited the highest antibacterial activity compared to the other samples. Along with the increase of pH value after Li doping in nano-MgO (10.93 *vs.* 11.00), the antibacterial activity become corresponding strengthen. The minimum inhibitory concentration (MIC) was decreased from 550 μg mL^{-1} to 500 μg mL^{-1}.[24] This is attributed to the Li doping strategy, which not only introduced oxygen vacancies but also enhanced the alkalinity of nano-MgO because Li is an alkali metal. Wang *et al.* and our latest work further indicated that the antibacterial activity of nano-MgO is not solely due to the increase in alkalinity but is most likely related to the high stability of ROS in slightly alkaline environments.[24,25] However, the study did not further investigate the trend of alkalinity of Li-doped nano-MgO in a simulated antibacterial environment as well as clarify the antibacterial contribution of ROS.

Ning and Ma *et al.* reported that Li-doped MgO nanoparticles have been successfully prepared by the microwave-assisted hydrothermal route and solution combustion route, respectively.[26,27] The results clearly showed that the antibacterial activity of MgO nanoparticles primarily depends on the enhancement of oxygen vacancies, which can lead to excessive production of ROS. Based on this, the equal volume impregnation–air calcination method was first employed in our synthesis system to enhance the antibacterial properties of nano-MgO, while eliminating the need to filter out the excess solution in another over-impregnation method, thereby reducing the loss of active components. Additionally, the contributions of alkalinity, ROS, physical morphology effect, and dissolved ions (Mg^{2+} and Li^{+}) to the antibacterial properties were discussed, and the antibacterial mechanism of Li-doped nano-MgO was also proposed. This study offers a novel approach to developing new and effective antibacterial MgO nanomaterials. Meanwhile, the antibacterial efficacy of the fabrics plays a crucial role in user health. Our previous studies primarily focused on magnesium based antibacterial agents and fabrics.[28,29] The results indicated that magnesium-based materials hold significant potential for the functional finishing of fabrics. However, the low antibacterial activity of pure MgO, along with unclear antibacterial mechanisms for Li doped nano-MgO, encouraged the authors to conduct this study to explore the contributions of oxygen vacancies and alkalinity in Li doped nano-MgO to enhance its activity and help to solve the antibacterial efficiency and stability issues of functional fabrics.

2. Experimental details

2.1 Synthesis method of Li-doped nano-MgO

The pure nano-MgO and Li-doped nano-MgO were synthesized using the hydrothermal-N_2 calcination method. Initially, 70 mL solution of magnesium chloride ($MgCl_2$) and ethylenediaminetetraacetic acid disodium salt (EDTA-2Na) were prepared with deionized water. 10 mL solution of ammonia was added as a precipitant. After stirring for 20 min at room temperature, the mixture was transferred to a teflon-lined stainless-steel autoclave and heated to 180 °C for 24 h. The precursor of nano-MgO was washed twice with deionized water and once with anhydrous ethanol, then dried at 60 °C for 8 h. Subsequently, Li-doped nano-MgO were prepared *via* equal volume impregnation method. The precursor of nano-MgO was added to a solution of lithium nitrate ($LiNO_3$) and was stirred for 10 min, and then left in a beaker for 8 h at room temperature. After impregnation, the white precipitate was dried at 50 °C for 10 h. Finally, the precipitate was calcined at 750 °C for 4 h under the air atmosphere. Based on the impregnant concentration (0.1, 0.5 and 1.5 wt%) of $LiNO_3$, Li-doped nano-MgO with different doping amounts were named 0.1Li-MgO, 0.5Li-MgO and 1.5Li-MgO, respectively. The pure nano-MgO was prepared using the same method without impregnation in a solution of $LiNO_3$. In this work, all reagents were purchased from Tianjin Kemiou Chemical Reagent without further purification.

2.2 Characterization techniques

X-ray diffraction (XRD) patterns of the samples were recorded on an X'Pert Pro diffractometer (USA) with Cu Kα ($\lambda = 1.5406$ Å) radiation. The scanning electron microscope (SEM) investigations of the samples were carried out with the help of a Hitachi S-4800 (Japan) with an accelerating voltage of 5 kV. The micrograph observations were also analyzed using a transmission electron microscopy (TEM, FEI Talos F200×, America). Thermo VG ESCALAB 250 X-ray photoelectron spectrometer (USA) was employed for X-ray photoelectron spectroscopy (XPS) studies, and then the spectra were calibrated referring to the C 1s peak at 284.6 eV.

2.3 Antibacterial studies

The plate count method was employed to test the antibacterial activity of pure and Li-doped nano-MgO against *Escherichia coli* (*E. coli*, ATCC 25922). 100 μg mL^{-1} of pure and Li-doped nano-MgO were respectively added to 10^5 CFU mL^{-1} of *E. coli* suspension and incubated in a shaking incubator at 37 °C. *E. coli* suspension without any MgO samples under the same conditions was used as blank control group. After 24 h, 100 μL of *E. coli* suspension was serially diluted using a PBS solution and spread on the surface of LB solid agar and followed by incubation at 37 °C for 24 h. Further, the antibacterial ratio of MgO samples was counted and calculated based on using formula (1):

$$\text{Antibacterial ratio } (\%) = \frac{A - B}{A} \times 100\% \quad (1)$$

where A and B are the number of *E. coli* colonies corresponding to the blank control and MgO sample groups. The biological reagents were purchased from Beijing Aoboxing Biotechnology.

The detailed methods were similar to the reported work by Ning *et al.*[26] Briefly, the *E. coli* suspension was diluted to

 © 2025 The Author(s). Published by the Royal Society of Chemistry

Open Access Article. Published on 19 February 2025. Downloaded on 5/4/2026 11:03:49 AM.
This article is licensed under a Creative Commons Attribution-NonCommercial 3.0 Unported Licence.

10^6 CFU mL^{-1} with LB liquid medium. The different samples (300 μg mL^{-1}) were added into the LB medium and then incubated at 37 °C in the shaking incubator with the speed of 150 rpm. The value was measured using a UV spectrophotometer (Shimadzu UV-2600, Japan) at a certain time and subsequently plotted to create a growth curve.

The live-dead studies of *E. coli* were detected using an acridine orange–propidium iodide (AO–PI) fluorescent double staining method. The suspension contained MgO samples and *E. coli* was cultured at 37 °C for 0 h and 12 h. After the suspension and 50 μL of the staining agent were fully mixed, the mixed suspension was dropped onto a glass slide and then the coverslip was covered on the slide. The live-dead of *E. coli* was analyzed by a fluorescence microscope.

2.4 Alkalinity tests

To evaluate the alkalinity change of Li-doped nano-MgO in the antibacterial environment, the simulating condition was conducted based on the antibacterial studies in the part of 2.3. The pure MgO and 1.5Li-MgO at 500 μg mL^{-1} were separately added to a PBS solution with the initial pH of 7.3 and then mixed for 5 min. The suspension of pure MgO and 1.5Li-MgO was separately shaken at 37 °C in a shaking incubator. Subsequently, the alkalinity change of pure MgO and 1.5Li-MgO was assessed by regularly monitoring the pH value.

2.5 ROS validation tests

100 μL of DCFH-DA solution was added into the *E. coli* suspension (10^5 CFU mL^{-1}) and incubated at 37 °C for 10 min. The 1.5Li-MgO was added to the DCFH-DA solution and was shaken for 20 min. After that, the above solution was washed with PBS solution. The fluorescence intensity was measured by fluorescence spectrophotometer (Cary Eclipse, America).

To test the generation of superoxide radical ions ($^{\bullet}O_2^-$), electron spin resonance (ESR) spectroscopy was conducted at room temperature. The detailed methods were similar to the previous literature reported by Ma *et al.*[27]

The 1.5Li-MgO at 100 μg mL^{-1} was added into the dialysis tube (MWCO of 12 000–14 000) and put into the *E. coli* suspension (10^5 CFU mL^{-1}) for incubation at 37 °C. The blank control group only received the equal amount of 1.5Li-MgO at 100 μg mL^{-1} without using the dialysis tubing. After 24 h, the antibacterial ratio was calculated based on formula (1). To further estimate the antibacterial contribution of dissolved Mg^{2+} and Li^+ from 1.5Li-MgO. Thus, the antibacterial activities of $MgCl_2$ and $LiNO_3$ from the raw materials at 100 μg mL^{-1} were tested by a plate count method.

3. Results and discussion

3.1 Characterization analysis

The undoped MgO and Li-doped nano-MgO were subjected to XRD analysis and the corresponding diffraction peaks were indicated by JCPDS card no. 45-0946, as shown in Fig. 1(a). The diffraction peaks of all samples appear at 36.9°, 42.8°, 62.3°, 74.6° and 78.6°, which correspond to the (111), (200), (220), (311) and (222) crystal planes, signifying the formation of cubic crystalline MgO. Compared with undoped MgO, Li-doped nano-MgO exhibited the additional peaks at 2θ values of 33.5° and 56.3°. The new peaks were denoted by an asterisk (*) in Fig. 1(a), which might be attributed to (111) and (220) crystal planes of Li_2O (JCPDS 12-0254), suggesting the presence of Li_2O. Furthermore, 0.5Li/MgO and 1.5Li/MgO displayed distinct diffraction peaks at 21.3°, 30° and 31.9°, which were attributed to the (020), (011) and (101) crystal faces of LiOH (JCPDS 25-0486), as shown in Fig. 1(b). The intensity of the diffraction peaks correspondingly increases with the amount of Li doping. The form of Li on the MgO surface was consistent with the findings of Raouf and Aritani *et al.*[30,31] Interestingly, a different phenomenon has been reported for the impurity phase of Li.[24,26] Other authors have found that the phase of Li_2CO_3 appears in the XRD pattern of MgO with increasing Li doping amounts. We inferred that the synthetic raw materials may influence the crystal structure of Li. The relationship between the synthetic raw materials and the form of Li present requires further investigation.

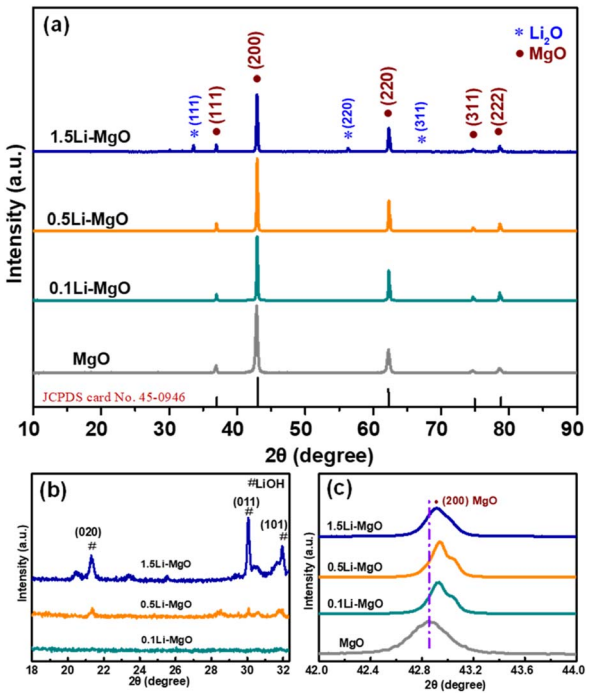

Fig. 1 (a) XRD patterns of MgO and Li-MgO, (b) the diffraction peak corresponding to Li phase and (c) the diffraction peak corresponding to (200) crystal plane.

As shown in Table S1 (ESI)† and Fig. 1(c), it can be observed that the FWHM correspondingly increased from 0.171° to 0.212° and the diffraction peaks at (200) of Li-doped nano-MgO shifted to a higher angle compared to that of pure MgO. A similar shift in the diffraction peak corresponding to the same crystal plane has been reported for Li-doped MgO.[26] According to Bragg's equation, the increase in the diffraction angle of MgO in relation to the decrease in *d*-spacing value might be attributed to atomic substitution. During the high-temperature

Open Access Article. Published on 19 February 2025. Downloaded on 5/4/2026 11:03:49 AM.
This article is licensed under a Creative Commons Attribution-NonCommercial 3.0 Unported Licence.

calcination process at 750 °C for 4 h, the substitution of Mg ions by Li ions in the MgO lattice readily occurred, indicating that additional Li ions were incorporated into the MgO lattice.[32,33] The lattice contraction might be due to atomic substitution reduced the interatomic interaction distance and enhanced the interactions, which might be beneficial for improving the activity of nano-MgO.[34] The ordered lattice structure of nano-MgO was effectively disrupted by Li doping, which would significantly impact the structural integrity of MgO crystalline phase and crystal size. According to the Debye-Scherrer formula,[35] the crystal sizes of Li-doped nano-MgO were smaller than that of pure MgO (49.3 nm), with sizes of 48.5 nm (0.1Li-MgO) > 44.9 nm (0.5Li-MgO) > 39.8 nm (1.5Li-MgO), respectively. There was a gradual decrease in *d*-spacing with an increase in Li doping levels. Conversely, there was an increase in FWHM as the Li content increased, indicating a progressive decrease in the crystallite size of nano-MgO, ranging from 49.3 to 39.8 nm. These changes in the microstructural parameters provided strong evidence that the lattice distortion in MgO generated by Li doping could inhibit the growth of host nanoparticles. Similar results have been reported for trends in the microstructural parameters of Zn-doped MgO synthesized using a solid-state reaction technique.[36,37]

The SEM images of the MgO and Li-MgO with different Li doping amounts are presented in Fig. 2. Both pure MgO and Li-doped nano-MgO exhibited a circular flake-like morphology with a diameter of approximately 200 nm and a thickness ranging from 10 to 20 nm. Although there was an increase in Li doping amounts, the morphology or particle size were not significantly changed. The results of TEM analysis were similar to the SEM. This phenomenon might be ascribed to the low doping concentration of Li. As shown in Fig. 3(c and d), the lattice fringe of pure MgO was highly ordered, which was ascribed to the perfect lattice of cubic phased MgO with high purity. However, some defects existed in the 1.5Li-MgO. This was sufficient to indicate that Li doping and high-temperature calcination are the driving forces for the lattice distortion of MgO. Many defects such as oxygen vacancies were also induced along with the creation of lattice distortion. Our results of TEM

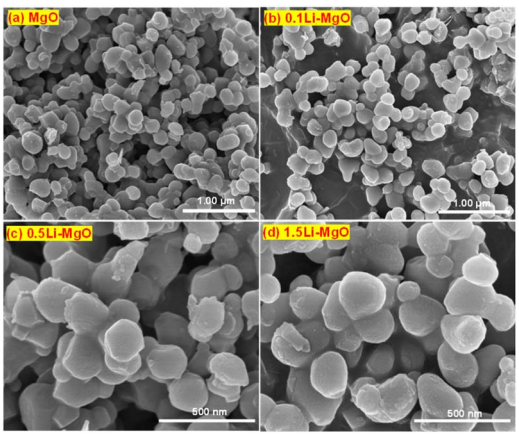

Fig. 2 SEM images of (a) MgO, (b) 0.1Li-MgO, (c) 0.5Li-MgO and (d) 1.5Li-MgO.

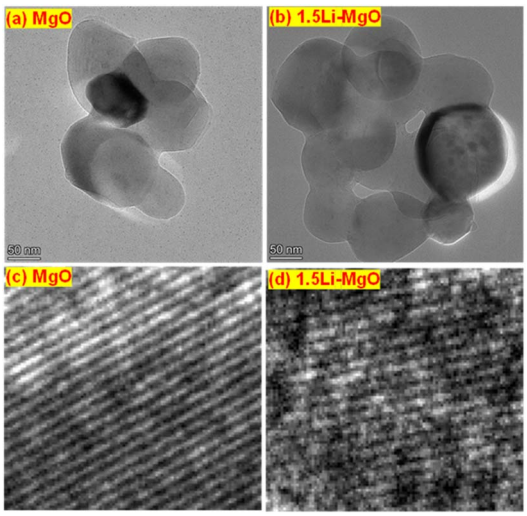

Fig. 3 TEM images of (a) MgO, (b) 1.5Li-MgO, (c) MgO and (d) 1.5Li-MgO.

were consistent with the reported literature.[38] The XRD and TEM results revealed that Li doping is a crucial strategy for influencing the lattice of nano-MgO and creating the defects.

The doping strategy of nano-MgO facilitates the introduction of oxygen vacancies. These vacancies have a significantly effect on the adsorbed oxygen content of nano-MgO. The surface chemical oxygen of MgO and Li-doped nano-MgO with varying Li doping amounts was further analyzed using XPS. In Fig. 4(a), the O 1s spectra of pure MgO were analyzed to identify lattice oxygen (O_L) and adsorbed oxygen (O_A). The characteristic peaks at low binding energies (529.1–529.7 eV) were attributed to O_L, while the peaks at high binding energies (531.2–531.8 eV) were attributed to O_A. In Fig. 4(b–d), the O_{III} characteristic peaks were observed in all Li-doped nano-MgO, which might be linked to the hydroxyl oxygen of LiOH.[39,40] Table S1 (ESI)† displays that 1.5Li-MgO exhibited the highest O_A content compared with

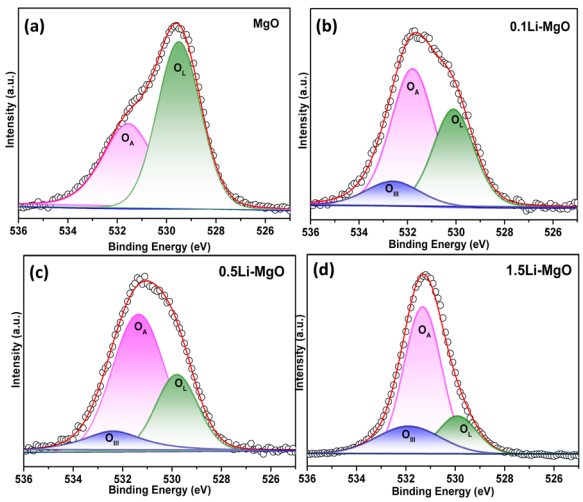

Fig. 4 O 1s XPS fine spectra of (a) MgO, (b) 0.1Li-MgO, (c) 0.5Li-MgO and (d) 1.5Li-MgO.

© 2025 The Author(s). Published by the Royal Society of Chemistry

Open Access Article. Published on 19 February 2025. Downloaded on 5/4/2026 11:03:49 AM.
This article is licensed under a Creative Commons Attribution-NonCommercial 3.0 Unported Licence.

pure nano-MgO, 0.1Li-MgO and 0.5Li-MgO, with increases of 11.1%, 9.2%, and 4.3%, respectively. The improved oxygen adsorption capability was attributed to the introduction of oxygen vacancies by distorting the MgO lattice based on Li doping strategy.

3.2 Antibacterial performance

To investigate the effect of Li doping on the antibacterial performance of nano-MgO, the antibacterial ratio of MgO and Li-MgO at 100 μg mL^{-1} was tested by a plate count method. As depicted in Fig. 5, the antibacterial ratio of 0.1Li-MgO was similar to that of pure MgO (86.5% *vs.* 84.4%). It was hypothesized that the low amount of Li doping was insufficient to disrupt the MgO lattice and introduce abundant oxygen vacancies. The XRD and XPS results also validated that the lattice parameter and O_A content of 0.1Li-MgO did not differ significantly from those of pure MgO. With an increase the amount of Li doping, the antibacterial performance of 0.5Li-MgO and 1.5Li-MgO was enhanced. Compared with 0.1Li-MgO and 0.5Li-MgO, 1.5Li-MgO exhibited the highest activity against *E. coli*, with the antibacterial ratio reaching 99.6%. And this result exceeded other reported by literature at same concentration.[27]

When the Li doping amount was low, the enhancement of antibacterial activity of MgO was relatively minor. As the Li doping amount increased from 0.1 wt% to 1.5 wt%, the antibacterial performance of MgO was significantly enhanced. This might imply that a low amount of Li doping was insufficient to disrupt the MgO lattice and introduce oxygen vacancies. An appropriate doping concentration of Li is essential for achieving the high antibacterial performance of nano-MgO. However, increased Li doping concentration dependence on antibacterial activity does not follow the same trend, as illustrated in Fig. S1(ESI).† Fewer surviving *E. coli* were observed on agar medium with 1.5Li-MgO (56 CFU mL^{-1}) compared to 3.0Li-MgO (417 CFU mL^{-1}) and 5.0Li-MgO (522 CFU mL^{-1}). This result indicated that a lower Li doping concentration promotes *E. coli* inactivation; however, when the concentration exceeds 1.5 wt%, it negatively impacts antibacterial activity. According to the XRD results, 1.5Li-MgO exhibited the impure phase of Li_2O. The high concentration of Li doping might cause an increase of the weight percentage of impurities in nano-MgO samples, thereby diminishing the antibacterial efficacy of nano-MgO.

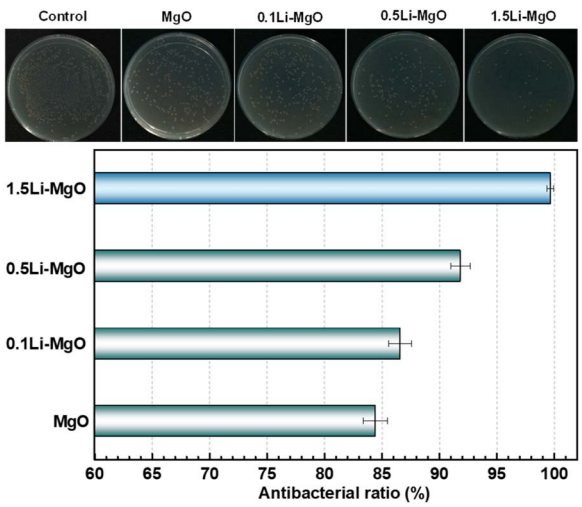

Fig. 5 Antibacterial activity of MgO and Li-MgO with different Li doping amounts.

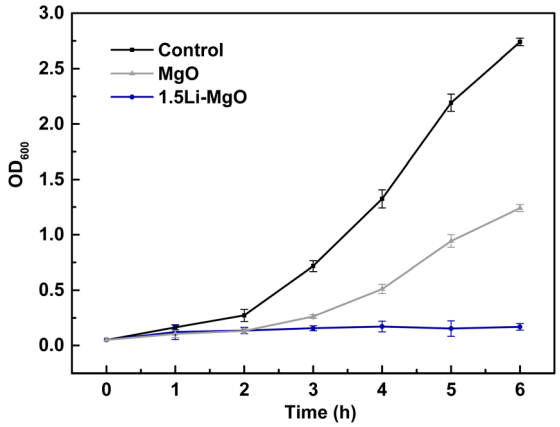

Fig. 6 The growth curves of *E. coli* respectively treated with MgO and 1.5Li-MgO.

Besides, Fig. 6 illustrates the growth curves of *E. coli* treated with MgO and 1.5Li-MgO. The 1.5Li-MgO revealed significantly inhibited the growth of *E. coli* compared to pure MgO counterpart. This result further demonstrated that a moderate amount of Li doping was an effective approach to enhance the antibacterial properties of nano-MgO.

To evaluate the live-dead *E. coli* treated with 1.5Li-MgO, a fluorescence microscope was used to record its live-dead staining state. As shown in Fig. 7(a), the field of vision was all green, suggesting that untreated *E. coli* exhibited normal activity, but the field of view revealed numerous red dots resulting from the treatment of 1.5Li-MgO after 12 h (Fig. 7(b)). The results clearly portrayed that more *E. coli* lose activity when in contact with 1.5Li-MgO, providing conclusive evidence that 1.5Li-MgO effectively destroyed the membrane, ultimately leading to *E. coli* death.

Fig. 8 presents the SEM images of *E. coli* surface morphology before and after exposure to 1.5Li-MgO. The untreated *E. coli* possessed solid normal morphology. However, the surface of *E. coli* treated with 1.5Li-MgO displayed distortion and wrinkles in

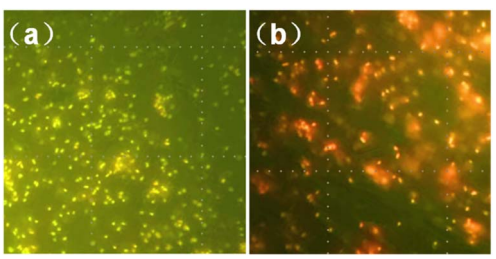

Fig. 7 Fluorescence micrograph of *E. coli* treated with 1.5Li-MgO for (a) 0 h and (b) 12 h.

Open Access Article. Published on 19 February 2025. Downloaded on 5/4/2026 11:03:49 AM.
This article is licensed under a Creative Commons Attribution-NonCommercial 3.0 Unported Licence.

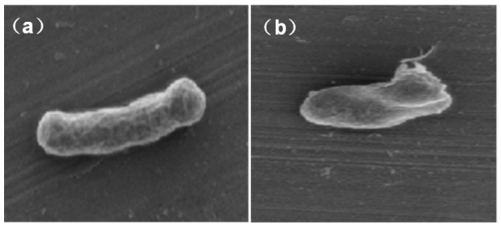

Fig. 8 SEM images of *E. coli* surface morphology before (a) and after (b) treatment with 1.5Li-MgO.

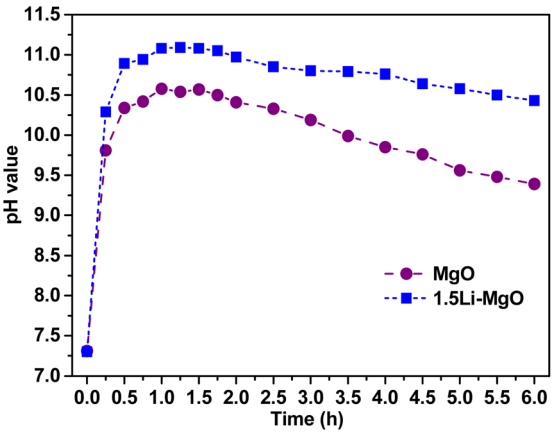

Fig. 9 Relationship between pH value and time of MgO and 1.5Li-MgO in a simulate antibacterial environment.

its morphological features. The results confirmed that 1.5Li-MgO could effectively damage *E. coli*.

In the previous report, the author proposed a new point that alkaline conditions are favorable for maintaining the stability of ROS in Li doped nano-MgO.[41] The work only examined the alkalinity of Li doped nano-MgO, without further assessing the alkalinity changes of the materials in the antibacterial environment. Herein, the pH-time variation of pure MgO and 1.5Li-MgO was investigated in a simulated antibacterial environment (in Fig. 9). The pH value of pure MgO and 1.5Li-MgO rapidly rose from 7.35 (the initial pH value) to peaks of 10.41 and 11.09 within 0–1.0 h, respectively. Subsequently, the pH value decreased slowly to 9.39 and 10.43 in 1.0–6.0 h. Importantly, the pH value of 1.5Li-MgO remained higher than that of pure MgO throughout the measurements. This disparity was attributed to two factors: (i) when doped into nano-MgO, Li as an alkali metal promots the increase of its alkalinity. (ii) The abundant oxygen vacancies created by Li doping act as the active sites that accelerating the hydrolysis of nano-MgO to produce more OH^-. Li doping effectively heightened the alkalinity of the antibacterial environment, enhancing the stability of ROS and bolstering the inactivation ability of nano-MgO against *E. coli*.

3.3 ROS validation analysis

To investigate the generation of ROS within *E. coli* treated by MgO and Li-MgO, the DCFDA staining study was tested and the fluorescence results were shown in Fig. 10. As the Li doping

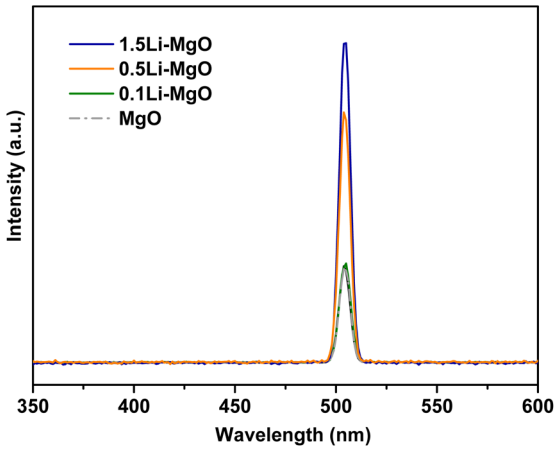

Fig. 10 The change of ROS levels in *E. coli* treated with MgO and Li-MgO based on DCFDA staining study.

level increased, the fluorescence intensity gradually rose. That meant more the presence of oxygen vacancies based on doping strategy, and higher the generation of ROS levels which was ultimately the explanation for enhancement in antibacterial activity with the Li doping levels increases from 0.1 wt% to 1.5 wt%.

The DCFDA staining studies was evident by enhancement in fluorescence intensity for the doped samples, indicating that the generated ROS accumulated in the bacteria. The $^{\bullet}O_2^-$ plays the greatest role among all single ROS in the antibacterial performance of nano-MgO. In Fig. 11, the obvious $^{\bullet}O_2^-$ signals of 1.5Li-MgO were captured by ESR, which directly demonstrated the generation of $^{\bullet}O_2^-$. The presence of oxygen vacancies, which was a major contributor to $^{\bullet}O_2^-$ generation, was essential for the antibacterial mechanism of nano-MgO.

ROS, as the strong oxidizing substance, have the characteristics of high reactivity and extremely short existence life. Accurate quantitative analysis of ROS remains a challenge. Additionally, the conversion generation among single ROS makes it more difficult to directly quantitatively detect ROS. In

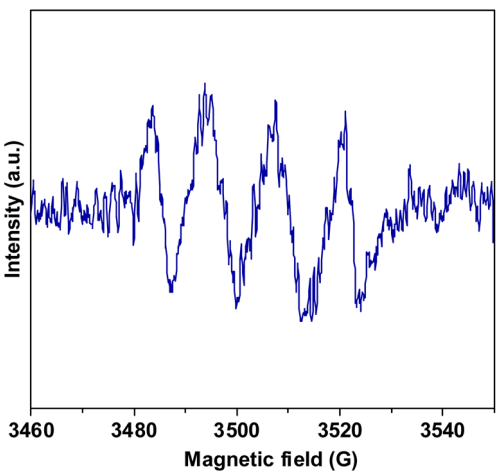

Fig. 11 ESR spectrum of the generation of $^{\bullet}O_2^-$ in 1.5Li-MgO.

© 2025 The Author(s). Published by the Royal Society of Chemistry

Open Access Article. Published on 19 February 2025. Downloaded on 5/4/2026 11:03:49 AM.
This article is licensed under a Creative Commons Attribution-NonCommercial 3.0 Unported Licence.

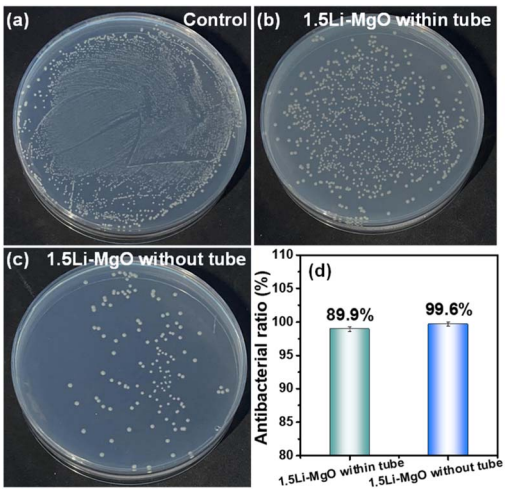

Fig. 12 Antibacterial activity of (a) control, (b) 1.5Li-MgO within tube, (c) 1.5Li-MgO without tube and (d) the antibacterial ratio.

this work, the dialysis tube was utilized to indirectly verify the antibacterial contribution of ROS. When the dialysis tube was used in the antibacterial test, MgO samples could not direct contact with *E. coli*, effectively avoiding the physical antibacterial effect.[42] Only ROS generated by oxygen vacancies and the dissolved ions can diffuse from the dialysis tube into the bacterial suspension to inactivate the bacteria. Based on the dialysis tube test, the antibacterial activity of two dissolved ions (Mg^{2+} and Li^{+}) was separately tested under the same antibacterial condition to indirectly clarify the contribution of ROS.

As shown in Fig. 12, the antibacterial ratio of 1.5Li-MgO without the dialysis tube reached 99.6% in direct contact with *E. coli*. After using the dialysis tube, its antibacterial ratio slightly decreased to 89.9% in indirect contact with *E. coli*. This result indicated indirectly that ROS, dissolved Mg^{2+} and Li^{+} diffused from the dialysis tube into the bacterial suspension might be the main factors affecting the antibacterial activity of

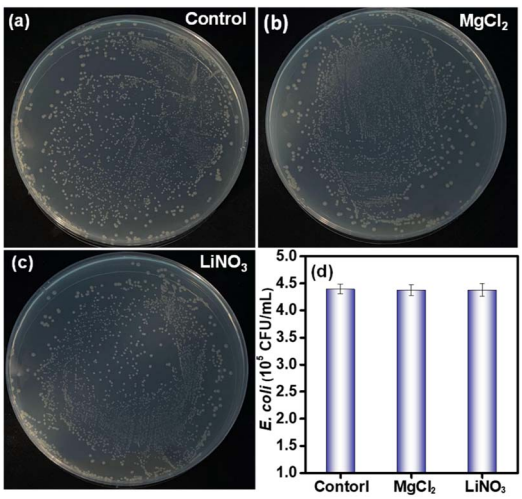

Fig. 13 Antibacterial activity of (a) control, (b) $MgCl_2$, (c) $LiNO_3$ and (d) the surviving colony number.

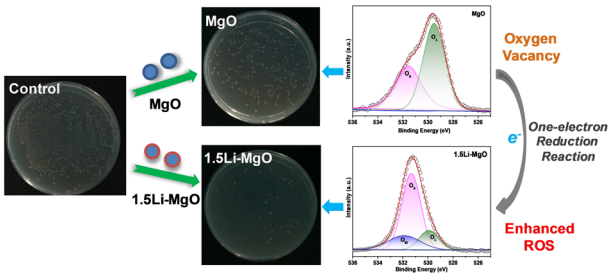

Fig. 14 Possible antibacterial mechanism of 1.5Li-MgO.

1.5Li-MgO. It is worth mentioning that the minor difference between two antibacterial ratios suggested that the physical direct contact contributed less to the antibacterial performance of 1.5Li-MgO. This was because 1.5Li-MgO had a smooth circular flake-like morphology with rounded edges, making it challenging to puncture and inactivate *E. coli* due to its physical morphology effect.[43]

Subsequently, the contribution of dissolved Mg^{2+} and Li^{+} to nano-MgO was assessed by a plate counting method. The raw materials $MgCl_2$ and $LiNO_3$ at 100 μg mL^{-1} were selected to evaluate the antibacterial activity of Mg^{2+} and Li^{+} (in Fig. 13). Compared to the surviving colony number of the control (4.39×10^5 CFU mL^{-1}), the surviving colony numbers treated with $MgCl_2$ and $LiNO_3$ were 4.38×10^5 and 4.39×10^5 CFU mL^{-1}, respectively, indicating almost no antibacterial contribution of dissolved Mg^{2+} and Li^{+}. Excluding the antibacterial effect of dissolved Mg^{2+} and Li^{+}, confirming that the excellent performance of 1.5Li-MgO was mainly due to the oxygen vacancies mediated ROS generation. The schematic diagram of the antibacterial mechanism was presented in Fig. 14. It can be seen that Li doping strategy caused MgO lattice distortion and increased oxygen vacancies, resulting in the enhancement of nano-MgO's ability to adsorb oxygen and induce the one-electron reduction reaction based on oxygen vacancies to generate more ROS, further improving the antibacterial activity of nano-MgO.

4. Conclusions

In this work, Li-doped nano-MgO were successfully prepared by the equal volume impregnation–air calcination method and were explored as the antibacterial agents with oxygen adsorption capacity to generate ROS, which exhibited the superior antibacterial activity against *E. coli*. Even a small amount of Li doping into nano-MgO could achieve the enhancement of its activity. Compared with pure MgO, the antibacterial efficacy of 1.5Li-MgO at 100 μg mL^{-1} against 10^5 CFU mL^{-1} *E. coli* increased from 84.4% to 99.6%. The enhancement was attributed to the lattice distortion of 1.5Li MgO and introduction of oxygen vacancies, resulting in the O_A content increase from 50.8% to 61.9%. And the increase of alkalinity in antibacterial environment from 10.41 to 11.09, which was favorable for the enhancement of generation and stability of ROS. The dialysis tube results further confirmed that ROS generated by oxygen

© 2025 The Author(s). Published by the Royal Society of Chemistry

Open Access Article. Published on 19 February 2025. Downloaded on 5/4/2026 11:03:49 AM. This article is licensed under a Creative Commons Attribution-NonCommercial 3.0 Unported Licence.

vacancies was the key factor contributing to the significant antibacterial effect of 1.5Li MgO. The physical direct contact contributed comparatively little to the antibacterial activity of nano-MgO, while the dissolved ions (Mg^{2+} and Li^{+}) had no contribution on its activity. The 1.5Li MgO shows promising potential in the field of antibacterial applications and public health safety. The fabrication of Li-doped nano-MgO by the equal volume impregnation–air calcination approach could accurately control the doping amount and diminish the pollution caused by the raw materials, which could be highly desirable to achieve efficient and green strategy for preparing of high-performance antibacterial materials. Additionally, Li doping strategy holds significant promise for inducing oxygen vacancies in nano-MgO and other metal oxides.

Data availability

The data that support the findings of this study are available from the corresponding author upon reasonable request.

Conflicts of interest

The authors declare that they have no known competing financial interests or personal relationships in this paper.

Acknowledgements

This work was financially supported by Yunnan Fundamental Research Projects (grant no. 202401AU070078), Scientific Research Fund of the Educational Department of Yunnan Province (grant no. 2024J0420) and Expert Workstation Project of Yunnan Province (grant no. 202305AF150042).

References

1 A. V. Singh, A. Katz, R. S. Maharjan, A. K. Gadicherla, M. H. Richter, J. Heyda, P. del Pino, P. Laux and A. Luch, *Sci. Total Environ.*, 2023, **860**, 160503.
2 D. Klingelhöfer, M. Braun, D. A. Groneberg and D. Brüggmann, *Emerging Microbes Infect.*, 2023, **12**, 202312.
3 A. A. Ali, R. D. Al Bostami and A. Al-Othman, *RSC Adv.*, 2024, **14**, 10546–10559.
4 A. Pandeya, Y. Zhang, J. Cui, L. Yang, J. Li, G. Y. Zhang, C. Q. Wu, Z. Y. Li and Y. A. Wei, *Microbiol. Res.*, 2023, **275**, 127460.
5 C. Y. Wang, S. L. Zhu, Y. Q. Liang, C. L. Qin, F. Wang, H. Wang, C. T. Chang and A. Inoue, *J. Colloid Interface Sci.*, 2023, **645**, 287–296.
6 F. G. Wang, S. Yang, Q. P. Lu, W. X. Liu, P. Sun, Q. Wang and W. B. Cao, *Colloids Surf., A*, 2023, **658**, 130741.
7 K. Ranathunga, P. Yapa, I. Munaweera, M. M. Weerasekera and C. Sandaruwan, *RSC Adv.*, 2024, **14**, 18536–18552.
8 R. Kumar, K. Seema, D. K. Singh, P. Jain, N. Manav, B. Gautam and S. N. Kumar, *J. Coord. Chem.*, 2023, **76**, 1065–1093.
9 X. Y. Li, Y. J. Liu, F. M. Wang, Y. P. Huang, X. Y. Feng, B. T. Zhu, Y. Z. Liu, Y. F. Qian, L. H. Lv and Y. Wang, *Surf. Interfaces*, 2023, **41**, 103171.
10 E. Ferrando-magraner, C. Bellot-arcís, V. Paredes-gallardo, J. M. Almerich-Silla, V. García-Sanz, M. Fernández-Alonso and J. M. Montiel-Company, *Medicina*, 2020, **56**, 1–23.
11 Y. J. Hao, B. Liu, L. G. Tian, F. T. Li, J. Ren, S. J. Liu, Y. Liu, J. Zhao and X. J. Wang, *ACS Appl. Mater. Interfaces*, 2017, **9**, 12687–12693.
12 O. Yamamoto, J. Sawai, H. Kojima and T. Sasamoto, *J. Mater. Sci.:Mater. Med.*, 2002, **13**, 789–792.
13 J. Xia, N. Zhang, Y. J. Yang, X. Chen, X. Wang, F. Pen and J. N. Yao, *Adv. Funct. Mater.*, 2023, **33**, 1–8.
14 A. Taser, M. E. Güldüren and H. Güney, *Mater. Chem. Phys.*, 2021, **272**, 124993.
15 X. Y. Hong, Y. Yang, X. Y. Li, M. Abitonze, C. S. Diko, J. A. Zhao, Q. A. Ma, W. F. Liu and Y. M. Zhu, *RSC Adv.*, 2021, **11**, 2892–2897.
16 J. N. D'Souza, G. K. Nagaraja, K. M. Navada, S. Kouser and D. J. Manasa, *Ceram. Int.*, 2021, **47**, 29620–29630.
17 B. Priyadarshini, B. P. Sahoo, T. Sahoo and T. R. Sahoo, *Mater. Lett.*, 2021, **304**, 130645.
18 R. Kayalvizhi, K. Neyvasagam, R. V. Shanthi and M. J. Abel, *Chem. Phys. Lett.*, 2022, **792**, 139384.
19 I. Apostolova, A. Apostolov and J. Wesselinowa, *Materials*, 2023, **16**, 2353.
20 P. Desai, V. Darji, M. P. Deshpande, S. H. Chaki, P. G. Sutariya, H. Soni, P. Solanki, N. A. Shah and B. Hirpara, *Mater. Chem. Phys.*, 2023, **299**, 127499.
21 P. Panchal, D. R. Paul, S. Gautam, P. Meena, S. P. Nehra, S. Maken and A. Sharma, *Chemosphere*, 2022, **297**, 134182.
22 A. Almontasser and A. Parveen, *Sci. Rep.*, 2022, **12**, 7922.
23 Y. Y. Rao, W. Wang, F. Tan, Y. C. Cai, J. W. Lu and X. L. Qiao, *Appl. Surf. Sci.*, 2013, **284**, 726–731.
24 Y. Rao, W. Wang, F. Tan, Y. Cai, J. Lu and X. Qiao, *Ceram. Int.*, 2014, **40**, 14397–14403.
25 X. Li, H. Liu, Y. He, Z. Li, F. Zhan, Y. Li and J. Zhao, *Ceram. Int.*, 2024, **50**, 42877–42885.
26 Q. Z. Tian, J. W. Ye, W. J. Yuan, S. Q. Zhang, L. Shi, J. C. Zhong and G. L. Ning, *Powder Technol.*, 2020, **371**, 130–141.
27 Z. Yin, X. Li, S. Li, W. Shi, A. Wang, J. Gao and C. Ma, *Ceram. Int.*, 2024, **50**, 1633–1642.
28 Y. Wang, J. Zhao, L. Sha, Y. Zhu and X. Li, *J. Mater. Sci.*, 2018, **53**, 1610–1622.
29 Y. Wang, L. Sha, J. Zhao, Q. Li, Y. Zhu and N. Wang, *Appl. Surf. Sci.*, 2017, **400**, 413–419.
30 F. Raouf, M. Taghizadeh and M. Yousefi, *React. Kinet., Mech. Catal.*, 2013, **110**, 373–385.
31 H. Aritani, H. Yamada, T. Nishio, T. Shiono, S. Imamura, M. Kudo, S. Hasegawa, T. Tanaka and S. Yoshida, *J. Phys. Chem. B*, 2000, **104**, 10133–10143.
32 T. Xin, L. J. Bai, G. T. Chen, G. J. Zhang and B. Zhao, *Surf. Interfaces*, 2024, **48**, 104289.
33 P. R. Moon, J. P. Kujur, A. Kumar and D. D. Pathak, *J. Mol. Struct.*, 2025, **1319**, 139602.

© 2025 The Author(s). Published by the Royal Society of Chemistry

Open Access Article. Published on 19 February 2025. Downloaded on 5/4/2026 11:03:49 AM.
This article is licensed under a Creative Commons Attribution-NonCommercial 3.0 Unported Licence.

34 C. Liu, C. Wu, X. Y. Tan, Y. Tao, Y. Zhang, D. Li, J. Yang, Q. Yan and Y. Chen, *Nat. Commun.*, 2023, **14**, 5597.
35 S. Varshney, A. Nigam, N. Mishra and S. J. Pawar, *J. Korean Ceram. Soc.*, 2023, **60**, 62–74.
36 R. Kumar and R. Kumar, *J. Mater. Sci.:Mater. Electron.*, 2024, **35**, 681.
37 R. Kant, Y. K. Agarwal, K. Kumar, S. Bansal and S. Kaul, *Mater. Technol.*, 2022, **37**, 3017–3024.
38 Z. R. Qiu, X. Y. Liu, T. Y. Yang, J. B. Wang, Y. Wang, W. L. Wenle and Y. Huang, *Adv. Funct. Mater.*, 2024, **34**, 2400220.
39 M. F. Chu, D. Q. Meng, Y. R. Li, M. Wang, S. Xiao, L. Z. Luo, X. C. Tang and S. L. Yang, *Appl. Surf. Sci.*, 2018, **447**, 673–676.
40 K. P. C. Yao, D. G. Kwabi, R. A. Quinlan, A. N. Mansour, A. Grimaud, Y. L. Lee, Y. C. Lu and S. H. Yang, *J. Electrochem. Soc.*, 2013, **160**, 824–831.
41 B. Abebe, E. A. Zereffa, A. Tadesse and H. C. A. Murthy, *Nanoscale Res. Lett.*, 2020, **15**, 190.
42 C. X. Dong, D. Song, J. Cairney, O. L. Maddan, G. H. He and Y. L. Deng, *Mater. Res. Bull.*, 2011, **46**, 576–582.
43 J. Das, C. Debnath, H. Nath and R. Saxena, *Energy Sources, Part A*, 2022, **44**, 4928–4938.

© 2025 The Author(s). Published by the Royal Society of Chemistry